PAPER

Assembly of a high-scattering photoelectrode using a hybrid nano-TiO$_2$ paste†

Jia Lin,[a] Li Zheng,[a] Xiaolin Liu,[b] Shu Zhu,[b] Yongsheng Liu[a] and Xianfeng Chen*[b]

The nanostructure architecture of photoanodes is a key factor in limiting the performance of dye-sensitized solar cells. In this study, TiO$_2$ nanotube (NT) powders were fabricated by the anodic growth of NT arrays on titanium foils followed by ultrasonic dispersion of the obtained NTs. The NTs were collected, annealed and then coated onto transparent conductive substrates to form pure NT photoanodes. The crystallinity of the NTs was optimized at a high annealing temperature. The highly crystallized NT powders were then incorporated into TiO$_2$ nanoparticle (NP) pastes to form NT–NP hybrid pastes; hybrid photoanodes were thus obtained. The embedded NTs served as a light-scattering component to trap the incident light inside the dye-sensitized TiO$_2$ films, leading to a significant enhancement in light absorption. By adjusting the weight ratio of the NT–NP hybrid pastes, the scattering effect could be optimized. The hybrid photoanode with the optimum film composition (50 wt% NT) gave the highest solar cell efficiency of 6.00% due to the simultaneous improvement in light scattering, dye anchoring and NT crystallinity. This fabrication strategy is simple, efficient, economical and suitable for use in large-scale production.

Introduction

The nanostructured photoanode is a very important component in typical dye-sensitized solar cells (DSSCs).[1,2] The functionality of the photoanode can be characterized primarily by three factors: the light-harvesting efficiency; the injection of electrons from the dyes to the semiconductor; and the electron collection. Typical photoanodes in DSSCs consist of a mesoporous TiO$_2$ metal oxide nanoparticle (NP) film, which provides a large accessible surface area on which to load the dye molecules and a unique band structure for efficient interfacial electron transfer. However, as a result of the limited lengths of electron diffusion and the small light absorption coefficients of the dyes, the photon energy of solar irradiation is not fully utilized. A significant portion of the incident light penetrates the NP film, especially in the long wavelength region.[3] An improvement in the light-harvesting capacity of the photoanode is therefore critical in the optimization of the solar energy conversion efficiency.

The nano-architecture of the photoelectrodes in DSSCs greatly influences the photon to electron performance. Much effort has been devoted to tuning the morphologies of the TiO$_2$ films or searching for alternative nanostructures that are

beneficial in improving the light absorption, charge collection and thus device performance. One representative strategy is the use of NP photoanodes containing light-scattering centers with a high diffuse reflectivity, such as large TiO$_2$ NPs (200–400 nm),[4,5] submicrometer-sized solid or hollow spheres,[6,7] core–shell structures,[8] one-dimensional rods/fibers/tubes,[9–13] and nano-patterning.[14,15] As a result of the wide-band scattering effect,[16] the incident light can be confined inside the solar cells, leading to enhanced light-harvesting efficiency over a broad spectral range. For various light-scattering structures, the improvement in dye adsorption, redox penetration and electron lifetime is essential to the high performance of the DSSCs.[7]

Vertically aligned one-dimensional anodic TiO$_2$ nanotube (NT) architectures have been developed for application in DSSCs. These architectures have many advantages, such as simple fabrication procedures, slow electron–hole recombination and enhanced carrier collection.[17–19] In addition, typical NTs have an inherent light-scattering ability as a result of their large outer diameters in the range 100–200 nm.[17,20,21] The light scattering can be even more prominent for designed submicron-sized large NTs.[22,23] However, as the NTs are grown on anodic Ti metal substrates, the NT layer has to be detached from the substrate to synthesize the free-standing NT film and then transferred and adhered onto the top of an NP film to act as a light-scattering layer.[24–27] In addition, the NT array suffers from a high concentration of defects, which is likely to induce many trap centers inside the NTs, resulting in poor charge collection and inferior DSSC performance.[28,29] To reduce the trap density, an enhancement

a Department of Physics, Shanghai University of Electric Power,
2103 Pingliang Road, Shanghai 200090, China
b Department of Physics and Astronomy, Shanghai Jiao Tong University,
800 Dongchuan Road, Shanghai 200240, China. E-mail: xfchen@sjtu.edu.cn
† Electronic supplementary information (ESI) available. See DOI: 10.1039/c5tc00860c.

This journal is © The Royal Society of Chemistry 2015

J. Mater. Chem. C, 2015, **3**, 6645–6651 | 6645

in the crystallinity of NTs by thermal treatment at a high temperature has been proposed, but the effectiveness of this is only guaranteed for free-standing NT films.[30]

Inspired by the various hybrid photoanodes consisting of one-dimensional TiO_2 nanostructures,[31,32] we report here a new and straightforward strategy to synthesize TiO_2 NTs in the powder form for use as light-scattering centers to improve the performance of solar cells. Without the influence of the underlying Ti substrate, highly crystallized NT powders can be obtained by a high-temperature thermal treatment. The efficiencies of the solar cells based on pure NT powders annealed at different temperatures were compared. The NT powders with optimized crystallinity were then integrated into conventional NP photoanodes to act as light-scattering assemblies. The dependence of the solar cell performance on the NT to NP ratio in the photoanode was investigated to achieve the best solar energy conversion efficiency.

Experimental

Preparation of NT powders and NT–NP hybrid paste

A two-step electrochemical anodization was used to grow NT arrays on a pure titanium foil substrate (99.7% purity, Alfa Aesar) with a thickness of 0.89 mm.[33,34] Anodization was carried out at a constant voltage of 60 V in a fluoride-containing ethylene glycol electrolyte with 0.5 wt% NH_4F and 3 vol% deionized (DI) water. The as-formed samples were ultrasonicated for 10 min in ethanol to strip off the NT oxide layer from the underlying Ti substrate. The anodization and ultrasonication processes were repeated until the foil was completely consumed. The NTs were then collected by centrifugation, washed three times with DI water and ethanol and then dried overnight under vacuum at 120 °C to obtain the NT powders. Finally, the powders were thermally treated at 550, 650 and 750 °C in air with heating and cooling rates of 2 °C min^{-1} for 2 h to induce crystallization, transforming the NTs into the pure anatase phase.

Two types of TiO_2 paste were synthesized. The type I pastes were composed of pure NT powders annealed at 550, 650 and 750 °C. The powders were added (10 wt%) to a 1 : 4 (v/v) mixture of isopropanol : n-butyl alcohol to prepare the pastes (designated as 550-NT, 650-NT and 750-NT). The type II pastes were composed of both NTs and NPs (hybrid pastes), prepared by adding the 650-NT paste to an NP paste (20 nm anatase, Dyesol 18NR-T). The NT to NP ratio in the pastes was controlled by adding different weight percentages of the 650-NT paste. The mixtures containing 1, 10, 20, 50 and 75 wt% NTs were designated as 1%-NT, 10%-NT, 20%-NT, 50%-NT and 75%-NT, respectively. The pure 650-NT sample with 100% NTs was designated as 100%-NT for comparison. The resultant pastes were well mixed under vigorous stirring at 200 rpm for 24 h before use. For comparison, an NP paste containing only NPs was also used to fabricate the reference photoanode (designated as 0%-NT).

Fabrication of photoanodes and solar cell assembly

The two types of TiO_2 paste were coated on fluorine-doped tin oxide (FTO) conducting glass (TEC-15, NSG) using a doctor-blade method. The resultant TiO_2 films were dried in air and then sintered at 450 °C for 2 h to form good mechanical contacts between the films and the substrates. The final thickness was about 8 μm for all the TiO_2 layers. After cooling down to approximately 80 °C, the TiO_2 photoanodes were immersed in an N719 dye solution (0.3 mM N719 in 1 : 1 (v/v) acetonitrile and tert-butanol; Solaronix) at room temperature for 24 h for sensitization.

For the assembly of the DSSCs, the sensitized TiO_2 electrode was rinsed with acetonitrile and dried in air. The electrode was then covered with Pt-coated FTO glass as the counter electrode and sealed with a 25 μm thick hot-melt film (SX1170-25; Solaronix) by heating at 120 °C. The Pt-coated FTO glass counter electrode was fabricated by spin-coating H_2PtCl_6 (10 mM in 2-propanol; Advanced) followed by thermal decomposition at 420 °C for 30 min. The interspace between the two electrodes was infiltrated using capillary force with a liquid redox electrolyte containing 1.0 M 1,2-dimethyl-3-propyl imidazolium iodide, 0.12 M diiodine, 0.1 M lithium iodide and 0.5 M 4-tert-butylpyridine in 3-methoxypropionitrile.

Structure and characterization of photovoltaic performance

The morphologies of the various TiO_2 nanostructured photoanodes were analyzed by field-emission scanning electron microscopy (FE-SEM; FEI Sirion 200). Transmission electron microscopy (TEM; JEOL JEM-2100F) was used to analyze the microstructure of the NTs. X-Ray diffraction (XRD, Cu Kα radiation; Rigaku 9KW SmartLab) was performed to verify the crystal structures. The Brunauer–Emmett–Teller (BET) surface areas were compared using nitrogen adsorption–desorption isotherms (ASAP 2010, Micromeritics). Samples for measurement were pre-treated at 200 °C for 4 h under high vacuum. The surface areas of the different photoanodes were also characterized by dye-desorption measurements. The dye molecules attached to the TiO_2 film surface were desorbed by placing in a 0.1 M NaOH aqueous solution for 5 min. The absorbance of the dye solution was measured by a UV-visible/NIR spectrophotometer (UV-3600, Shimadzu) to evaluate the dye-loading capacity. The transmittance and diffuse reflectance spectra of the photoanodes were also obtained using the UV-visible/NIR spectrophotometer.

The corresponding power conversion efficiencies (PCEs) of the assembled DSSCs were determined by a source meter (Model 2420, Keithley) under full sunlight (AM 1.5G, 100 mW cm^{-2}) with an irradiated active area of 0.16 cm^2. A class A solar simulator (450 W; Model 94023A, Newport-Oriel Instruments) was used with an AM 1.5 filter and the light intensity was calibrated using a silicon reference cell (Mono-Si with KG filter; NIST). The incident photon-to-current conversion efficiency (IPCE) spectra in the range 400–800 nm were measured using an IPCE measurement kit (Newport-Oriel Instruments) under short-circuit conditions. Electrochemical impedance spectrometry (EIS) in the frequency range 0.1 Hz to 100 MHz was carried out in the dark with an electrochemical workstation (CHI 660C, CH Instruments). The applied bias voltage was the same as the open-circuit voltage of the solar cells, which was modulated by a small amplitude voltage of 10 mV. The capacitance and resistance

were determined by fitting the impedance spectra to a simple equivalent circuit.

Results and discussion

To take advantage of the scattering effect of the NTs and to facilitate their incorporation, we fabricated NT powders, pure NT photoanodes and NT–NP hybrid photoanodes. Fig. 1 is a schematic diagram of the fabrication process. First, aligned NT arrays were grown on a Ti foil substrate by electrochemical anodization. The NTs were densely packed with a film thickness of about 20 μm (Fig. S1, ESI†). The as-formed NTs were then ultrasonically dispersed in ethanol and collected to synthesize the NT powders. The powders were thermally treated at various temperatures to induce crystallization. Finally, the crystallized powders were made into NT pastes, followed by coating directly onto FTO glass substrates to form type I electrodes. A hybrid NT–NP paste was also obtained by adding the NT paste to a conventional NP paste. We deposited this paste onto FTO glass substrates to form type II hybrid electrodes.

The embedded NTs acted as light-scattering centers in the type II electrode configuration. When the incident light reached the hybrid photoanode, the light was scattered and trapped inside the TiO_2 layer, extending the effective light path in the solar cells. As a result, the recycling of the light inside the photoanode strengthened the capture and utilization of photon energy. The incorporation of the NT scattering centers inside the NP films has many advantages compared with typical double-layered photoanodes, in which the scattering capacity results from the deposition of a separate scattering layer on the top of a TiO_2 NP film.[4,9,35] These advantages include simple synthesis procedures and excellent physical/electrical contacts between the NT and NP components.

The nanostructured morphology of the NT powder is shown in Fig. 1. This SEM image shows that the as-formed closely packed NT arrays were well dispersed into randomly fragmented NTs, which had lengths in the sub-micrometer to several micrometers range. Fig. 2 shows the morphological variation in the
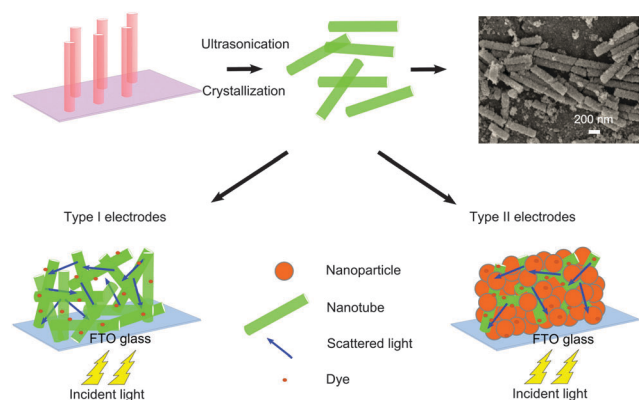

Fig. 2 SEM images of the NT powder samples annealed at (a, d) 550 °C, (b, e) 650 °C and (c, f) 750 °C showing the morphological evolution with annealing temperature.
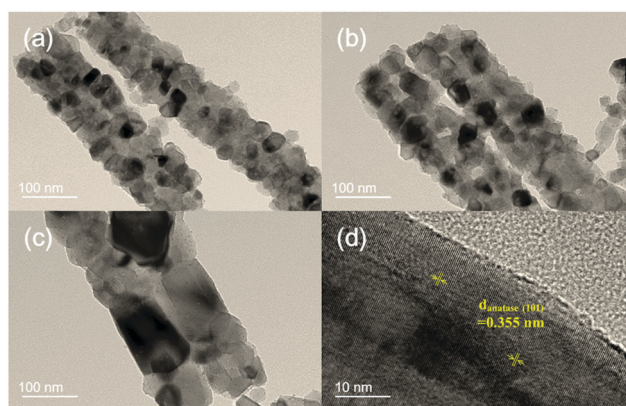
Fig. 3 TEM images of NTs annealed at (a) 550 °C, (b) 650 °C and (c) 750 °C. (d) Corresponding HRTEM image showing the crystallites in the walls of an NT.

Fig. 1 Schematic representation of the fabrication process for the NT powders and two different types of photoanodes (type I, pure NTs; type II, NT–NP composites). The corresponding SEM image of the randomly accumulated NTs in the powder form is also shown.
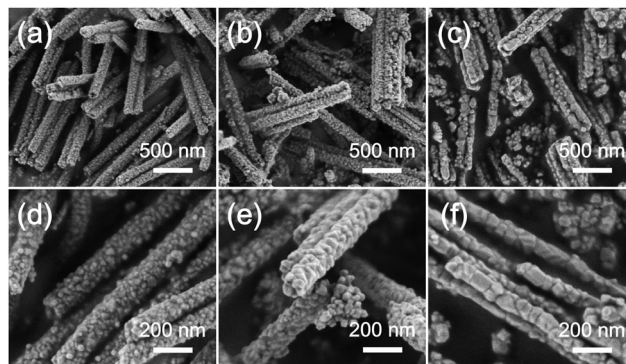
NT powders with increasing annealing temperature. The tubular architecture was maintained at all temperatures. However, a slight change in structural integrity was observed for the samples treated at 750 °C, with the appearance of some broken or consolidated tubes. The one-dimensional structure of the NTs was further demonstrated in the TEM images (Fig. 3). After high-temperature crystallization, we can clearly observe large and elongated nano-crystallites in the tube walls. For the NTs annealed at 750 °C, the tubes were partially fragmented (Fig. 3c). Compared with the TiO_2 NT bundles fabricated by the detachment, annealing and grinding of the NT array films[36] or by the rapid breakdown anodization method,[37,38] the NT powders obtained here were of high quality. According to the XRD patterns (Fig. 4), the diffraction peaks of all the NT samples after annealing at 550, 650 and 750 °C can be indexed to the anatase phase. In particular, the intensity of the anatase (101) peak increased gradually, indicating an improved degree of crystallization. The HRTEM image in Fig. 3d also gives a closer inspection of the nano-crystallites with apparent anatase (101) lattice fringes. The results indicate that, after the high-temperature annealing, the crystallinity of the NTs could be greatly enhanced, which is believed to be helpful in improving charge collection and solar cell performance.
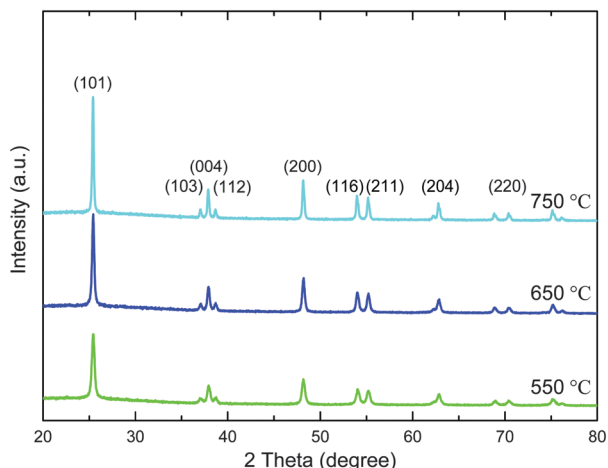
Fig. 4 XRD patterns of the NT powders annealed at different temperatures.
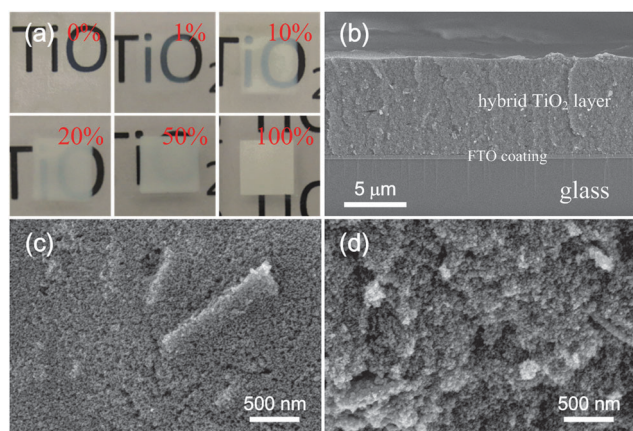

Fig. 5 (a) Photographs of the photoanodes with different NT to NP ratios showing various film transparencies. (b) Cross-sectional SEM image of the hybrid NT–NP photoanode. The high magnification (c) top-view and (d) side-view SEM images show the NTs embedded in the NP network.

By utilizing the NTs in the powder form, we can easily control the NT to NP ratio of the hybrid paste by incorporating different amounts of NTs into the NP pastes. Visually, the photoanode composed of a typical NP film without any scattering component showed high transparency in the visible range (0%-NT; Fig. 5a). The NPs have negligible light-scattering effects because the size of the NPs is much smaller than the wavelength of visible light. In contrast, with increasing percentages of NTs (1%-NT, 10%-NT and 20%-NT) introduced into the NPs, the film transparency gradually decreased and the photoanode became semi-transparent. After the coupling of high concentrations of NTs (50%-NT and 100%-NT), the NT–NP hybrid photoanode became non-transparent. These results demonstrate that the NTs had a good scattering ability over the visible region and that the scattering efficiency was greatly affected by changing the NT to NP ratio.

The cross-sectional SEM image of Fig. 5b shows that the hybrid NT–NP film fabricated by this strategy was homogeneous, compact and crack-free. The uniform thickness film was well connected to the conducting FTO glass substrate. The top-view

SEM image indicates that the hybrid film had a flat and regular top surface (Fig. 5c). The NTs were randomly distributed after being embedded in the NP network. Fig. 5d shows a side-view SEM image of the hybrid film. As the spaces among the NTs could be infiltrated with NPs, small voids were found inside the photoanode. The TEM image of the NT–NP hybrid paste is shown in Fig. S2 (ESI†). However, in the photoanodes based on pure NT (Fig. S3, ESI†), large-sized NT aggregates were loosely stacked, creating many large voids inside the photoanodes. This hinders electron transfer between the neighboring NTs and decreases the specific surface area.

To evaluate the scattering effect of the NTs on the enhancement of the solar cell efficiency, the photocurrent density–photovoltage (I–V) characteristics of pure NT films (type I) and the NT–NP hybrid films with different NT to NP ratios (type II) were investigated (Fig. 6a). First, the dependence of the type I solar cell efficiencies on the heat treatment temperatures was considered. By increasing the temperature, both the photocurrent density and the efficiency were improved. The DSSCs based on the NTs annealed at 650 °C (650-NT) showed an optimized PCE of 3.34%. Without the influence of Ti metal substrate, improved NT crystallinity can be obtained by heat treatment at a high temperature. The highly crystallized NTs enhanced charge collection and the efficiency of the solar cells.[30,39] However, for pure NT samples,
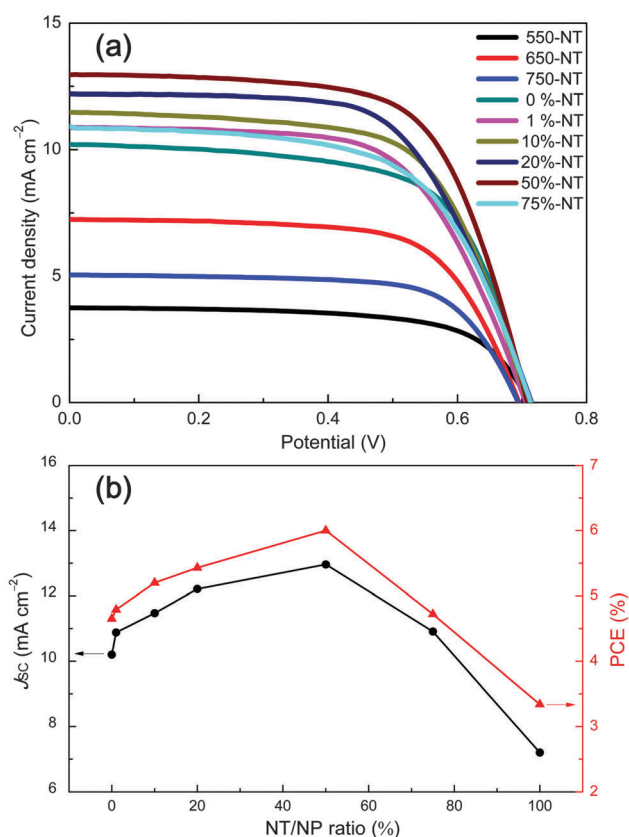

Fig. 6 (a) Photocurrent density–photovoltage characteristics of the DSSCs based on type I and type II electrodes. (b) Dependence of the short-circuit current density and solar cell efficiency on the NT to NP ratio in the electrode.

6648 | J. Mater. Chem. C, 2015, 3, 6645–6651

This journal is © The Royal Society of Chemistry 2015

the optimized cell efficiency (3.34%) remained much lower than that of the reference NP solar cell (0%-NT) with a similar thickness, which showed a PCE of 4.65%. The NT aggregates in the pure NT electrodes (type I) were loosely connected, resulting in small internal surface areas, low dye adsorption and slow electron diffusion through the films, which had a negative effect on the performance of the solar cells.

Given that the NT powders annealed at 650 °C had the optimum crystallinity, we then mixed these powders with NPs at different ratios to fabricate the NT–NP hybrid photoanodes. The photovoltaic performances of the DSSCs based on these photoanodes are also shown in Fig. 6a. The photocurrent densities gradually increased with increasing NT to NP ratios up to 50%, leading to improved PCEs. The NT–NP hybrid solar cell with 50 wt% NTs (50%-NT) showed the highest short-circuit current density (J_{SC}) of 12.96 mA cm^{-2}, an open-circuit voltage (V_{OC}) of 0.71 V, a fill factor (FF) of 65.3% and the highest PCE of 6.00%. For comparison, the pure NP cell (0%-NT) with a similar thickness showed a J_{SC} value of 10.20 mA cm^{-2}, a V_{OC} of 0.71 V, an FF of 64.2% and a PCE of 4.65%. The NT–NP hybrid solar cell showed a maximum increase in PCE of approximately 29% compared with the solar cell based on the pure NPs. The V_{OC} showed little change for all the samples and was in the range 0.69–0.71 V. However, for higher NT to NP ratios (75%-NT and 100%-NT), the efficiency sharply decreased, primarily because of the poor structure of the electrodes, which were mainly composed of NTs. Unlike previously reported results with optimized concentrations of 5–10% NTs,[11,12] increasing the NT ratio here played a positive role in boosting the efficiency. This may be attributed to the highly crystallized and high-quality NTs with multiple functions in the enhancement of the solar cell performance. The variations in J_{SC} and PCE as a function of the NT to NP ratio are shown in Fig. 6b and the detailed photovoltaic parameters are summarized in Table 1.

We further compared the amounts of dye adsorbed on these different configurations of photoanodes by dye-desorption experiments. The amounts of dye loaded per unit electrode area for the 550-NT and 650-NT samples were similar, whereas that of the 750-NT sample decreased significantly (Fig. 7). Because the tubes in the pure NT photoanodes were loosely packed, many large pores or voids existed inside the film and thus the amounts of dye loaded were all very low. The BET specific surface areas
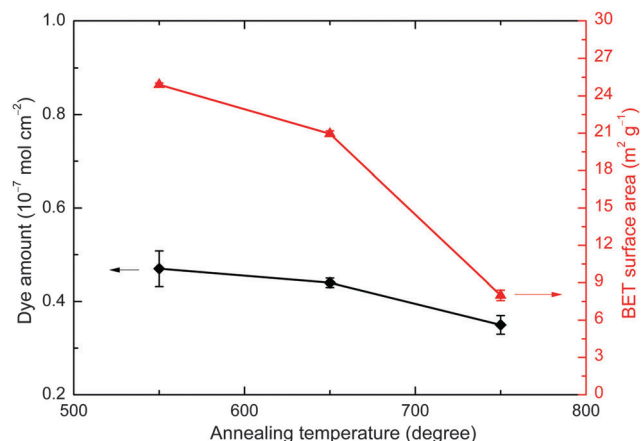

Fig. 7 Amount of dye-loaded on type I NT photoanodes and the BET surface areas of NT powders annealed at different temperatures.

of the NT powders annealed at 550, 650 and 750 °C were determined by nitrogen-sorption analysis and were 24.9, 21.0 and 8.0 m^2 g^{-1}, respectively (Fig. 7). The variation in the surface areas was consistent with that of the amounts of dye loaded, with a sharp decrease in surface area for the 750 °C sample. Although the morphology and phase of the NTs remained stable after annealing at 750 °C, the tubes were more or less fused together (the inner small pores disappeared), leading to much less internal surface area being accessible to the dye molecules.

Among the different photoanodes, the amount of dye loaded was largest for the conventional NP photoanode. As the surface area of pure the NTs was smaller than that of the NPs,[40] the incorporation of the NTs affected the dye-loading capacity of the hybrid photoanodes. The amount of dye adsorbed on the hybrid photoanodes slowly decreased with increasing NT content. Compared with the NP photoanode, the lower loading of the dye on the hybrid photoanodes caused decreased light harvesting. This drawback could be overcome by the significant light scattering of the NTs in the solar cells, which resulted in enhanced light harvesting overall and thus improved the photocurrent densities and solar cell efficiencies.

The external quantum efficiencies from the IPCE spectra confirmed the enhancement of the photocurrent densities of the NT–NP hybrid photoanodes. Fig. 8a shows that the 50%-NT sample had a much higher quantum efficiency than the pure NP (0%-NT) solar cell over the entire wavelength region (400–800 nm). In detail, the peak efficiency increased from 55% for the 0%-NT sample to 62% for the 50%-NT sample at a wavelength of 530 nm. A recent analysis has shown a superior electron diffusion length in the highly crystallized NTs compared with the conventional NTs and NPs.[30] Efficient electron collection through the highly crystallized NTs incorporated in the photoanode was responsible for the enhanced efficiency. It was also noted that the efficiency gap between the 0%-NT and 50%-NT samples was greater in the longer wavelength region from 600 to 800 nm. This was attributed to the superior light-scattering capability of the NTs embedded in the NP films, especially at long wavelengths. In particular, it is clearly shown in Fig. 8a that although the peak efficiency for the

Table 1 Photovoltaic parameters and amounts of adsorbed dye in DSSCs based on pure NTs annealed at 550–750 °C and NT–NP hybrid films with NT to NP ratios in the range 0–75%

Device	J_{SC} (mA cm^{-2})	V_{OC} (V)	FF (%)	PCE (%)	Dye amount × 10^{-7} (mol cm^{-2})
550-NT	3.76	0.71	65.3	1.75	0.47
650-NT (100%-NT)	7.20	0.70	66.8	3.34	0.44
750-NT	5.06	0.69	69.1	2.42	0.35
0%-NT	10.20	0.71	64.2	4.65	1.00
1%-NT	10.88	0.71	62.4	4.79	0.98
10%-NT	11.47	0.71	64.1	5.20	0.93
20%-NT	12.21	0.71	62.2	5.43	0.89
50%-NT	12.96	0.71	65.3	6.00	0.80
75%-NT	10.91	0.71	60.8	4.72	0.63

This journal is © The Royal Society of Chemistry 2015

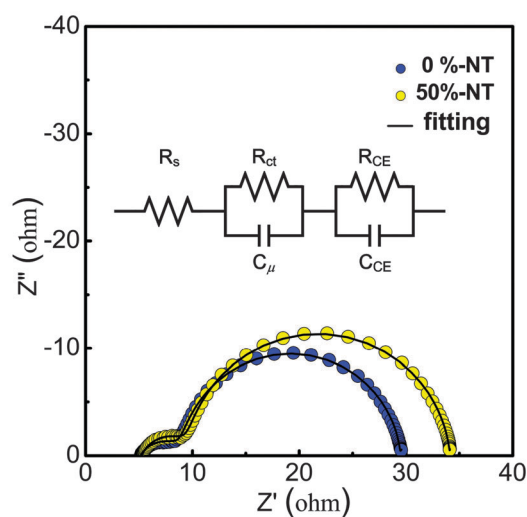J. Mater. Chem. C, 2015, 3, 6645–6651 | 6649

Fig. 9 EIS Nyquist plots under open-circuit conditions of the 0%-NT and 50%-NT samples. The plots were fitted with an equivalent circuit shown in the insert.

Table 2 Interfacial resistances and capacitances of DSSCs based on the 0%-NT and 50%-NT photoanodes[a]

Device	R_s (Ω)	R_{ct} (Ω)	C_μ (mF cm^{-2})	R_{CE} (Ω)	C_{CE} (mF cm^{-2})
0%-NT	5.12	19.55	2.36	4.02	0.76
50%-NT	5.25	24.02	1.91	4.39	0.40

[a] R_s = series resistance; R_{ct} and C_μ = resistance/capacitance at the TiO$_2$/electrolyte interface; R_{CE} and C_{CE} = resistance/capacitance at the counter electrode/electrolyte interfaces; τ_n = electron lifetime.

Fig. 8 (a) IPCE spectra of the hybrid NT–NP structures with NT to NP ratios of 0, 50 and 100%. (b) Transmission spectra of the samples with 0, 1, 10, 20 and 50% NT concentrations.

pure NT photoanodes was much lower, the efficiency at longer wavelengths was comparable with that of the pure NPs. This suggests that the strong scattering effect of the NTs can promote the absorption of long wavelength light inside the photoanodes and thus enhance the photocurrent densities of the solar cells.

When the NTs were integrated into the NP films, the film transparency significantly decreased with increasing NT content. This can also be observed from the light transmission spectra of these films (Fig. 8b). For example, introducing 1% NTs into the NP film would lead to a 33% decrease in the film transparency at 530 nm. When the NT to NP ratio in the hybrid film exceeded 50%, the film exhibited a very low transmittance and almost no light could be transmitted through the photoanode. The diffuse reflectance spectra of the photoanodes with 0–100% NTs provide further evidence of the strong scattering effect of the NTs (Fig. S4, ESI†). With increasing NT ratios in the hybrid films, the light reflectance increased gradually over the whole visible range of 400–800 nm. In particular, the peak reflectance of the 50%-NT sample was around 66%, much higher than that of the NP electrode (22%). As a result, the NTs embedded in the NPs are suitable for improving the light harvesting in DSSCs.

The electrochemical behavior of the NT–NP hybrid solar cells was analyzed by EIS.[41] Fig. 9 shows the Nyquist plots from the

EIS studies, which were fitted using the equivalent R_s–R_{ct}/C_μ–R_{CE}/C_{CE} circuit shown in the inset. It can be directly observed that the radius of the semicircle at intermediate frequencies (the main arc) of the 50%-NT sample was larger than that of 0%-NT sample. This indicates an increase in the electron transfer resistance (R_{ct}) and a reduction in the electron recombination rate with the oxidized species at the TiO$_2$/electrolyte interfaces for the NT–NP cell with respect to the NP cell. According to the fitting results (Table 2), the R_{ct} of the NT–NP solar cell showed a higher value (24.02 Ω) than that of NP solar cell (19.55 Ω). It was also found that the chemical capacitance (C_μ) of the NT–NP electrode (1.91 mF cm^{-2}) was lower than that of the NP electrode (2.36 mF cm^{-2}), which implies lower defect centers and/or trap density in the highly crystallized 650-NT sample.[42] The apparent electron lifetime (τ_n) can thus be estimated by the equation $\tau_n = R_{ct}C_\mu$. The result shows that the values of τ_n in the 650-NT solar cell was similar to that in the NP solar cell (45.9 ms for the NT–NP cell vs. 46.1 ms for the NP cell), which is consistent with the similar V_{OC} observed in the solar cells.

Conclusions

We have developed a new kind of nanostructured photoanode containing TiO$_2$ NPs and NTs for efficient light harvesting in high-performance DSSCs. The NT powders can be readily

6650 | J. Mater. Chem. C, 2015, 3, 6645–6651

This journal is © The Royal Society of Chemistry 2015

fabricated by electrochemical anodization and ultrasonic dispersion. The NT powders were made into a paste and then coated onto FTO glass substrates to fabricate the pure NT photoanodes. The crystallinity of the NT powders was optimized to obtain the highest DSSC efficiency. The NT paste was also mixed with NP paste to synthesize an NT–NP hybrid paste and the corresponding NT–NP hybrid photoanodes. This hybrid configuration showed pronounced light-scattering effects, a high dye-loading capacity and efficient electron collection. Suitable adjustment of the NT to NP ratios in the photoanodes maximized the light-harvesting properties of the DSSCs. Despite the 33% lower amount of dye loaded, the PCEs of the solar cells based on the hybrid photoanodes were improved by up to 29% compared with the conventional NP devices.

Acknowledgements

Notes and references

1 B. O'regan and M. Grätzel, *Nature*, 1991, **353**, 737.
2 B. E. Hardin, H. J. Snaith and M. D. McGehee, *Nat. Photonics*, 2012, **6**, 162.
3 H. J. Snaith and L. Schmidt-Mende, *Adv. Mater.*, 2007, **19**, 3187.
4 S. Ito, T. N. Murakami, P. Comte, P. Liska, C. Grätzel, M. K. Nazeeruddin and M. Grätzel, *Thin Solid Films*, 2008, **516**, 4613.
5 S. Hore, C. Vetter, R. Kern, H. Smit and A. Hinsch, *Sol. Energy Mater. Sol. Cells*, 2006, **90**, 1176.
6 I. G. Yu, Y. J. Kim, H. J. Kim, C. Lee and W. I. Lee, *J. Mater. Chem.*, 2011, **21**, 532.
7 S. Dadgostar, F. Tajabadi and N. Taghavinia, *ACS Appl. Mater. Interfaces*, 2012, **4**, 2964.
8 J. Feng, Y. Hong, J. Zhang, P. Wang, Z. Hu, Q. Wang, L. Han and Y. Zhu, *J. Mater. Chem. A*, 2014, **2**, 1502.
9 H.-Y. Chen, T.-L. Zhang, J. Fan, D.-B. Kuang and C.-Y. Su, *ACS Appl. Mater. Interfaces*, 2013, **5**, 9205.
10 S. H. Hwang, C. Kim, H. Song, S. Son and J. Jang, *ACS Appl. Mater. Interfaces*, 2012, **4**, 5287.
11 J. Sheng, L. H. Hu, S. Y. Xu, W. Q. Liu, L. e. Mo, H. J. Tian and S. Y. Dai, *J. Mater. Chem.*, 2011, **21**, 5457.
12 A. Lamberti, A. Sacco, S. Bianco, M. Quaglio, D. Manfredi and C. F. Pirri, *Microelectron. Eng.*, 2013, **111**, 137.
13 D. A. Wang, B. Yu, F. Zhou, C. W. Wang and W. M. Liu, *Mater. Chem. Phys.*, 2009, **113**, 602.
14 X. Zhang, H. Liu, X. Huang and H. Jiang, *J. Mater. Chem. C*, 2015, **3**, 3336.
15 S. Wooh, H. Yoon, J. H. Jung, Y. G. Lee, J. H. Koh, B. Lee, Y. S. Kang and K. Char, *Adv. Mater.*, 2013, **25**, 3111.
16 Y.-J. Chang, E.-H. Kong, Y.-C. Park and H. M. Jang, *J. Mater. Chem. A*, 2013, **1**, 9707.
17 K. Zhu, N. R. Neale, A. Miedaner and A. J. Frank, *Nano Lett.*, 2007, **7**, 69.
18 D. B. Kuang, J. Brillet, P. Chen, M. Takata, S. Uchida, H. Miura, K. Sumioka, S. M. Zakeeruddin and M. Grätzel, *ACS Nano*, 2008, **2**, 1113.
19 C.-T. Yip, H. T. Huang, L. M. Zhou, K. Y. Xie, Y. Wang, T. H. Feng, J. Li and W. Y. Tam, *Adv. Mater.*, 2011, **23**, 5624.
20 L. L. Li, C. Y. Tsai, H. P. Wu, C. C. Chen and E. W. G. Diau, *J. Mater. Chem.*, 2010, **20**, 2753.
21 H. G. Yun, J. H. Park, B. S. Bae and M. G. Kang, *J. Mater. Chem.*, 2011, **21**, 3558.
22 X. Liu, M. Guo, J. Lin, X. Chen and H. Huang, *RSC Adv.*, 2014, **4**, 45180.
23 Y. Zhang, J. Khamwannah, H. Kim, S. Y. Noh, H. Yang and S. Jin, *Nanotechnology*, 2013, **24**, 045401.
24 Q. Zheng, H. Kang, J. Yun, J. Lee, J. H. Park and S. Baik, *ACS Nano*, 2011, **5**, 5088.
25 J. Luo, L. Gao, J. Sun and Y. Liu, *RSC Adv.*, 2012, **2**, 1884.
26 X. Liu, M. Guo, J. Cao, J. Lin, Y. H. Tsang, X. Chen and H. Huang, *Nanoscale Res. Lett.*, 2014, **9**, 362.
27 X. K. Xin, J. Wang, W. Han, M. D. Ye and Z. Q. Lin, *Nanoscale*, 2012, **4**, 964.
28 Y. Yu, K. J. Wu and D. L. Wang, *Appl. Phys. Lett.*, 2011, **99**, 192104.
29 P. Docampo, S. Guldin, U. Steiner and H. J. Snaith, *J. Phys. Chem. Lett.*, 2013, **4**, 698.
30 J. Lin, M. Guo, C. T. Yip, W. Lu, G. Zhang, X. Liu, L. Zhou, X. Chen and H. Huang, *Adv. Funct. Mater.*, 2013, **23**, 5952.
31 B. Tan and Y. Wu, *J. Phys. Chem. B*, 2006, **110**, 15932.
32 P. Joshi, L. Zhang, D. Davoux, Z. Zhu, D. Galipeau, H. Fong and Q. Qiao, *Energy Environ. Sci.*, 2010, **3**, 1507.
33 J. Lin, J. F. Chen and X. F. Chen, *Electrochem. Commun.*, 2010, **12**, 1062.
34 G. Zhang, H. Huang, Y. Zhang, H. Chan and L. Zhou, *Electrochem. Commun.*, 2007, **9**, 2854.
35 T. Deepak, G. Anjusree, S. Thomas, T. Arun, S. V. Nair and A. S. Nair, *RSC Adv.*, 2014, **4**, 17615.
36 C.-J. Lin, W.-Y. Yu and S.-H. Chien, *Appl. Phys. Lett.*, 2007, **91**, 233120.
37 N. F. Fahim and T. Sekino, *Chem. Mater.*, 2009, **21**, 1967.
38 K. S. Lee, J. Kwon, J. H. Im, C. R. Lee, N.-G. Park and J. H. Park, *ACS Appl. Mater. Interfaces*, 2012, **4**, 4164.
39 T. Zeng, H. Ni, X. Su, Y. Chen and Y. Jiang, *J. Power Sources*, 2015, **283**, 443.
40 A. Kongkanand, K. Tvrdy, K. Takechi, M. Kuno and P. V. Kamat, *J. Am. Chem. Soc.*, 2008, **130**, 4007.
41 R. Kern, R. Sastrawan, J. Ferber, R. Stangl and J. Luther, *Electrochim. Acta*, 2002, **47**, 4213.
42 C. Di Valentin, G. Pacchioni and A. Selloni, *J. Phys. Chem. C*, 2009, **113**, 20543.

This journal is © The Royal Society of Chemistry 2015

J. Mater. Chem. C, 2015, **3**, 6645–6651 | **6651**